Journal of
Applied Crystallography
ISSN 1600-5767

The strongly defective double perovskite $Sr_{11}Mo_4O_{23}$: crystal structure in relation to ionic conductivity

Carlos A. López, José C. Pedregosa, Diego G. Lamas and José A. Alonso

J. Appl. Cryst. (2014). **47**, 1395–1401

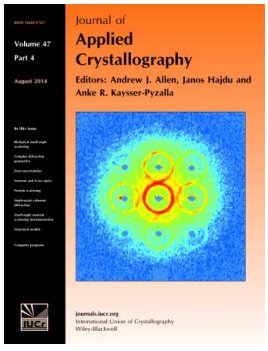

Journal of
Applied Crystallography
ISSN 1600-5767

Received 30 March 2014
Accepted 10 June 2014

The strongly defective double perovskite $Sr_{11}Mo_4O_{23}$: crystal structure in relation to ionic conductivity

Carlos A. López,[a]* José C. Pedregosa,[a] Diego G. Lamas[b] and José A. Alonso[c]

[a]INTEQUI–CONICET and Área de Química General e Inorgánica 'Dr G. F. Puelles', Facultad de Química, Bioquímica y Farmacia, Universidad Nacional de San Luis, Chacabuco y Pedernera, 5700 San Luis, Argentina, [b]CONICET and Laboratorio de Caracterización de Materiales, Facultad de Ingeniería, Universidad Nacional del Comahue, Buenos Aires 1400, (8300) Neuquén Capital, Provincia de Neuquén, Argentina, and [c]Instituto de Ciencia de Materiales de Madrid, CSIC, Cantoblanco, 28049 Madrid, Spain. Correspondence e-mail: calopez@unsl.edu.ar

The crystal structure and ionic conductivity properties of a novel microcrystalline $Sr_{11}Mo_4O_{23}$ ceramic material are presented. This material has been prepared by thermal treatment up to 1473 K, in air, of previously decomposed citrate precursors. The complex crystal structure was refined from combined X-ray powder diffraction and neutron powder diffraction data. The formula of this phase can be rewritten as $Sr_{1.75}\square_{0.25}SrMoO_{5.75}$, highlighting the relationship with double perovskites $A_2B'B''O_6$. At room temperature, the crystal structure is tetragonal in space group $I4_1/a$, with a = 11.6107 (6) Å, c = 16.422 (1) Å and V = 2213.8 (2) Å^3. The crystal network contains O anion and Sr cation vacancies. The structure is complex, with Sr, Mo and O atoms distributed over four, two and six distinct Wyckoff sites, respectively. Only one of the Sr sites (SrO_6) corresponds to the octahedral network; one of the two MoO_6 types of octahedra is axially distorted. The three other Sr positions occupy the A site with higher coordination. There is an occupational deficit of O atoms of 22 (4)%. This defective framework material presents an interesting ionic mobility, enhanced above 773 K owing to a further reduction in the oxygen content.

1. Introduction

In the field of materials chemistry, transition metal oxides are currently of significant interest for the development of renewable energy technologies such as solid oxide fuel cells, thermoelectric modules and high-temperature superconductors (Rao & Raveau, 1998; Raveau, 2007). Fuel cells are among the most promising devices for environmentally clean energy production by directly converting chemical energy into electricity (Steele & Heinzel, 2001; Kartha & Grimes, 1994). Among them, solid oxide fuel cells (SOFCs) have the unique capability of using a variety of fuels such as hydrocarbons or hydrogen (Singhal & Kendal, 2003). However, several issues have to be solved in order to improve their efficiency and cost of operation. Reduction of the typically high working temperature, which is around 1173–1273 K, is one of the most important issues, in order to avoid degradation problems due to thermal cycling or diffusion at interfaces and to reduce the cost of the interconnection materials. For this reason, extensive research has been devoted in recent years to the study of novel materials and structures to produce cells capable of working as intermediate-temperature solid oxide fuel cells (IT-SOFCs). In this investigation it is of paramount importance to unveil the details of the crystal structure in relation to the ionic motion, such as order–disorder transitions, lattice defects, cationic and/or anionic deficiencies, tilting of polyhedra, anisotropic thermal displacements *etc.* This knowledge is essential to establish relationships between the structures and the macroscopic phenomenology, with the final aim of optimizing the properties of interest.

In particular, perovskite oxides (ABO_3) have been protagonists in the field of energy-conversion materials. It is well known that double perovskite oxides ($A_2B'B''O_6$) can be derived from the simple ABO_3 perovskite structure by the introduction of two B-site cations arranged in a rock-salt fashion. Some of these materials have an ideal cubic structure, although most present distortions. The most common are the octahedral tilting distortions, which occur when the A-site cation is too small to fill the cuboctahedral cavity within the $B'B''O_6$ framework. When this is the case, the $B'O_6$ and $B''O_6$ octahedra rotate as nearly rigid units, thereby maintaining the B'—O and B''—O distances while allowing for shorter A—O distances.

It is generally assumed that the possible modes of octahedral tilting are limited by the fact that the corner-sharing connectivity of the $(B',B'')O_6$ network must be maintained. While almost all known perovskites obey this restriction, in the past few years there have been reports of compounds

where the corner-sharing connectivity is not maintained (Abakumov *et al.*, 2009). This only occurs when there is a very large difference in ionic radius (Δr_i) between the B' and B'' cations and a small tolerance factor. The required size mismatch was evaluated as Δr_i = 0.50–0.66 Å for the $A_2B'B''O_6$ double perovskites (King *et al.*, 2010).

Although the majority of structures with broken corner-sharing connectivity of the octahedral framework are fluorides or oxyfluorides, nothing prevents mixed oxides from adopting such a structure. So far, only the A-site deficient perovskites $A_{1.75}\square_{0.25}B'B''O_6$ (where $A = B'$ and $\square$ denotes a vacancy in the A sublattice) are known, where a rotation of 50% of the small $B''O_6$ octahedra by ~45° raises the coordination number of all the B' cations to 8. The known compounds with this structure are $Sr_{11}Os_4O_{24}$, $Ca_{11}Re_4O_{24}$, $Sr_{11}Re_4O_{24}$ and $Ba_{11}Os_4O_{24}$ (Tomaszewska & Müller-Buschbaum, 1993; Jeitschko *et al.*, 1998; Bramnik *et al.*, 2000; Wakeshima & Hinatsu, 2005). A few years ago, a new perovskite with this structure was reported, where A-site deficiency is observed together with oxygen vacancies ($Ba_{11}W_4O_{23}$ or $Ba_{1.75}\square_{0.25}BaWO_{5.75}\square_{0.25}$) (Hong, 2007). These vacancies generate an ionic conductivity, which was investigated and reported by Ha *et al.* (2008). Ionic conductivity through oxygen vacancies at high temperature makes these materials suitable for use as electrolytes in SOFCs, oxygen sensors and oxygen pumps.

Several molybdate-based ceramic materials which might be useful as components in SOFCs have also been described (Graves *et al.*, 2010). The first major material based on Mo that was studied for use in SOFCs was the oxide ion conductor $La_2Mo_2O_9$ (Lacorre *et al.*, 2000). This material was found to have higher O^{2-} ion conductivity than yttria-stabilized zirconia (YSZ) at temperatures above 873 K, suggesting that it could be a good electrolyte material. However, it is unstable in reducing atmospheres in this temperature range, limiting its practical applicability. Many other Mo-containing oxides with double-perovskite or pyrochlore structures (Graves *et al.*, 2010) have been reported to show promising properties as either anodes or electrolytes for SOFCs.

In this work we combine the $A_{11}B_4O_{23}$ framework with the appealing properties of Mo in SOFC materials. We describe for the first time the synthesis of $Sr_{11}Mo_4O_{23}$ by a citrate method, and its complex crystal structure is studied by combined X-ray powder diffraction (XRPD) and neutron powder diffraction (NPD). We also investigate the ionic conductivity and its relation to the crystal structure in microcrystalline ceramics. In addition, the effect of temperature is analysed by FT–IR spectroscopy, differential scanning calorimetry, thermogravimetric analysis and thermal expansion measurements.

2. Experimental

$Sr_{11}Mo_4O_{23}$ was prepared as a brown polycrystalline powder from citrate precursors obtained by soft chemistry procedures. Stoichiometric amounts of analytical grade $Sr(NO_3)_2$ and $(NH_4)_6Mo_7O_{24}{\cdot}4H_2O$ were dissolved in citric acid. The citrate and nitrate solutions were slowly concentrated, leading to organic resins containing a random distribution of the cations involved at an atomic level. These resins were first dried at 453 K and then slowly decomposed at temperatures up to 873 K. All the organic materials and nitrates were eliminated in a subsequent treatment at 1073 K for 2 h in air, giving rise to highly reactive precursor materials. The resulting brown powder was then treated in air at 1273 K for 24 h and fired at 1473 K in two periods totalling 12 h, and finally the sample was furnace-cooled to room temperature.

The initial identification and characterization of the sample was carried out by XRPD. The experimental patterns were obtained on a Rigaku D-MAX-IIIC diffractometer with Cu $K\alpha$ (λ = 1.5418 Å) radiation; the 2θ range was 10–120° in increments of 0.02° and the counting time was 5 s per step. To study the crystallographic structure at room temperature (295 K), NPD patterns were collected on the HRPT diffractometer of the SINQ spallation source (Paul Scherrer Institute, Villigen, Switzerland) with a wavelength of 1.494 Å. Both XRPD and NPD diffraction patterns were analysed in a combined refinement with the Rietveld method using the *FULLPROF* program (Rietveld, 1969; Rodríguez Carvajal, 1993).

Thermogravimetric analysis (TGA) and differential scanning calorimetry (DSC) curves were obtained using a Stanton STA 781 instrument. The temperatures of the peaks were measured with an accuracy of ±1 K. Analyses were carried out in an air flow at a heating rate of 1 K min^{-1}. About 50 mg of powder sample was used in each case.

The FT–IR spectra were measured by transmittance techniques between 4000 and 300 cm^{-1} and recorded on a Nicolet Protege 460 FT–IR instrument with 32 scans, using the KBr pellet technique.

Measurement of the thermal expansion coefficient (TEC) and electrical conductivity required the use of sintered pellets of 6 mm diameter, heated in air at 1473 K for 12 h. The obtained density is around 90–95% of the crystallographic density. Thermal expansion of the sintered samples was performed in a Linseis L75HX1000 dilatometer between 373 and 1273 K in air, with a heating rate of 5 K min^{-1}.

The electrical conductivity was measured by two-probe electrochemical impedance spectroscopy from 473 to 1173 K in dry air using an Autolab PGSTAT 302N potentiostat/galvanostat with an FRA2 frequency-response analyser module. The frequency range was 0.1–10^6 Hz. For these measurements, Pt electrodes were applied on both sides of the sintered pellets by painting with a commercial paste and firing at 1223 K for 1 h.

3. Results

3.1. Crystallographic structure

The structural refinement was performed from combined XRPD and NPD data. At room temperature, this compound presents a cation-deficient structure where the corner-sharing connectivity of the octahedral framework is broken. The crystal structure is defined in the tetragonal space group $I4_1/a$, and it is isostructural with the strontium rhenate perovskite

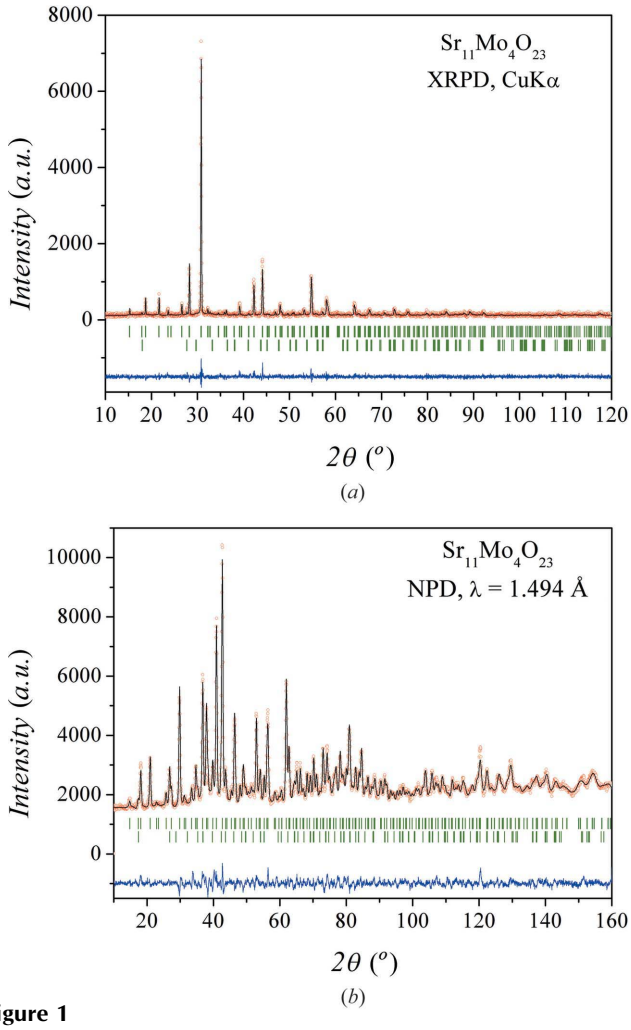

Figure 1
(*a*) Room-temperature X-ray powder diffraction data (red circles) and Rietveld calculated line profiles (solid black line) for $Sr_{11}Mo_4O_{23}$ complex perovskite. The blue line at the bottom is the difference between the calculated and experimental patterns for each sample. The upper set of green bars corresponds to the Bragg reflections for the main phase and the lower set of bars to the Bragg reflections for the $SrMoO_4$ impurity phase. (*b*) Rietveld plot (solid black line) after refinement of the crystal structure of $Sr_{11}Mo_4O_{23}$ complex perovskite from NPD data (red circles). The blue line at the bottom is the difference between calculated and experimental patterns. The sets of green bars correspond to the Bragg reflections for the major $Sr_{11}Mo_4O_{23}$ and impurity $SrMoO_4$ phases.

$Sr_{11}Re_4O_{24}$ (Bramnik *et al.*, 2000). A minor amount of $SrMoO_4$ was detected as an impurity and included in the refinement with its crystal structure defined in the space group $I4_1/a$. From the scale factor of the main and secondary phases we estimated the impurity level as 5 (1) wt%. The good agreement between the observed and calculated XRPD and NPD patterns after the refinements is shown in Figs. 1(*a*) and 1(*b*), respectively. The structural parameters at room temperature are listed in Tables 1 and 2.[1] Fig. 2 shows different projections of the $Sr_{11}Mo_4O_{23}$ crystal structure along the [100], [001] and [110] axes.

[1] Supporting information for this paper is available from the IUCr electronic archives (Reference: PD5046).

Table 1
Crystallographic data for the $Sr_{11}Mo_4O_{23}$ phase from combined refinements of XRPD and NPD data at 295 K.

System: tetragonal; space group: $I4_1/a$, Z = 4. Unit-cell parameters: a = 11.6107 (6) Å, c = 16.422 (1) Å and V = 2213.8 (2) Å^3.

Atom	Wyckoff site	x	y	z	B_{iso}	Occupancy
Sr1	4*a*	0	0.25	0.125	2.4 (4)	1
Sr2	8*e*	0.5	0.25	0.611 (1)	3.5 (5)	1
Sr3	16*f*	0.219 (1)	0.979 (1)	0.871 (1)	1.7 (2)	1
Sr4	16*f*	0.216 (1)	0.237 (1)	0.526 (1)	1.5 (2)	1
Mo1	8*c*	0	0	0	0.8 (2)	1
Mo2	8*d*	0	0	0.5	1.0 (2)	1
O1	16*f*	0.872 (1)	0.137 (1)	0.259 (1)	0.5 (2)	1
O2	16*f*	0.636 (2)	0.133 (2)	0.242 (2)	2.3 (4)	1
O3	16*f*	0.275 (1)	0.256 (2)	0.364 (1)	0.2 (2)	1
O4	16*f*	0.837 (1)	0.172 (1)	0.656 (1)	0.7 (3)	0.79 (4)
O5	16*f*	0.867 (2)	0.088 (2)	0.500 (2)	6.9 (8)	1
O6	16*f*	0.313 (2)	0.170 (3)	0.662 (2)	6.0 (8)	1

For NPD data: R_p = 0.134, R_{wp} = 0.175, R_{exp} = 0.0782, χ^2 = 5.01 and R_{Bragg} = 0.0481. For XRPD data: R_p = 0.133, R_{wp} = 0.174, R_{exp} = 0.0777, χ^2 = 4.99 and R_{Bragg} = 0.125.

Table 2
Main distances and angles in the $Sr_{11}Mo_4O_{23}$ structure (Å, °).

Sr1—O1 ×4	2.97 (2)	Sr3—O1	2.74 (2)	Sr4—O1	2.59 (2)
Sr1—O2 ×4	3.02 (2)	Sr3—O1	2.85 (2)	Sr4—O2	2.42 (2)
Sr1—O3 ×4	2.61 (1)	Sr3—O2	2.82 (3)	Sr4—O3	2.75 (2)
		Sr3—O2	2.76 (3)	Sr4—O4	2.62 (2)
Sr2—O1 ×2	2.60 (2)	Sr3—O3	2.73 (2)	Sr4—O4	2.46 (2)
Sr2—O2 ×2	2.68 (3)	Sr3—O3	2.49 (2)	Sr4—O5	2.29 (3)
Sr2—O3 ×2	3.20 (2)	Sr3—O4	2.66 (2)	Sr4—O6	2.61 (3)
Sr2—O5 ×2	3.33 (3)	Sr3—O5	2.64 (3)	Sr4—O6	3.18 (3)
Sr2—O6 ×2	2.50 (3)	Sr3—O6	2.48 (3)		

Mo1—O1 ×2	1.93 (1)	Mo2—O4 ×2	2.05 (2)
Mo1—O2 ×2	1.90 (2)	Mo2—O5 ×2	1.85 (2)
Mo1—O3 ×2	1.91 (1)	Mo2—O6 ×2	1.87 (3)
⟨Mo1—O⟩	1.92 (1)	⟨Mo2—O⟩	1.92 (1)
Δ(Mo1—O)	0.47×10^{-4}	Δ(Mo2—O)	21.35×10^{-4}
O1—Mo1—O2	92 (1)	O1—Mo2—O2	96 (2)
O1—Mo1—O3	91 (1)	O1—Mo2—O3	100 (2)
O2—Mo1—O3	94 (1)	O2—Mo2—O3	101 (2)

3.2. TGA and DSC measurements

Fig. 3 illustrates the TGA and DSC curves in air for an $Sr_{11}Mo_4O_{23}$ sample. The thermal events observed can be separated into three zones. In the low-temperature zone, up to 573 K, an endothermic weight-loss process is observed around 363 K. In the medium zone there is a complex process consisting of two mass losses accompanied by endothermic peaks at around 673 and 848 K. These processes appear to be reversible, since an exothermic mass gain is observed in the cooling curve which begins at 823 K. Finally, in the third zone, an endothermic non-reversible process is shown at 1053 K. We note that these changes are very subtle; all mass changes are about 2%.

Therefore, some subtle reversible and non-reversible processes occur when the sample is treated thermally. In order to identify these processes, FT–IR measurements were carried out before and immediately after the heat treatment.

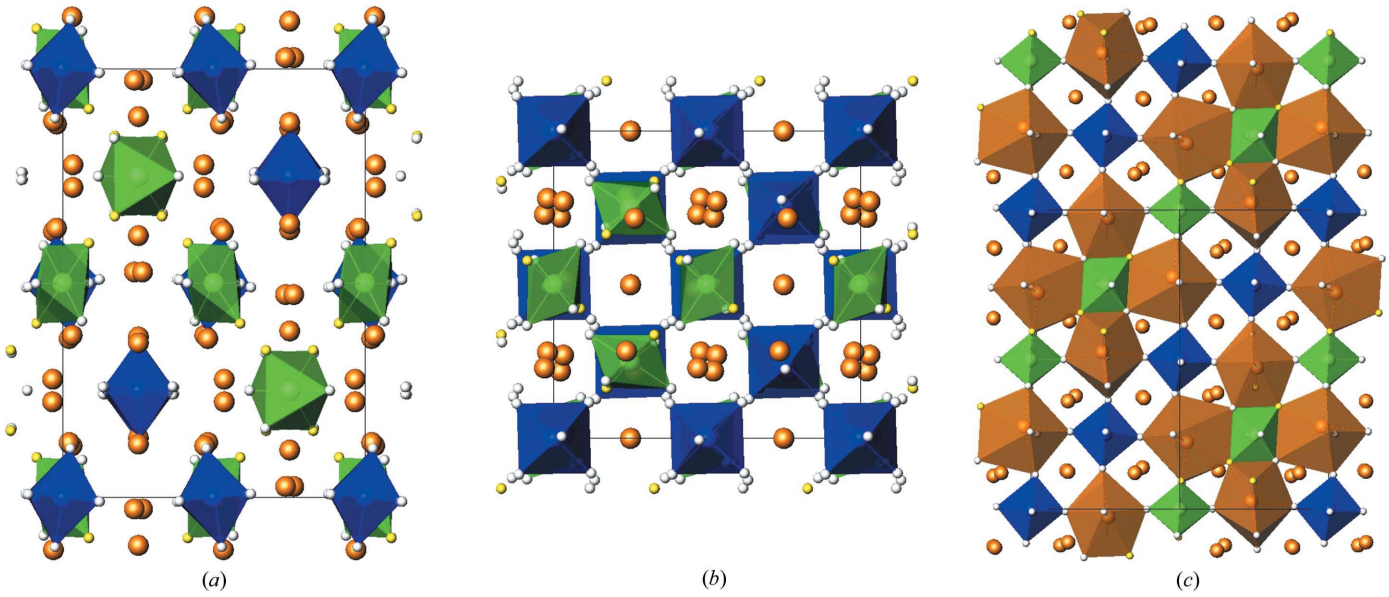

Figure 2
Different projections of the crystal structure of $Sr_{11}Mo_4O_{23}$ along (*a*) the [100], (*b*) the [001] and (*c*) the [110] axes. Mo1 and Mo2 atoms are represented as blue and green polyhedra, respectively, and Sr4 as brown polyhedra (in *c*). The O atom with vacancies (O4) is shown as yellow spheres and the rest as white spheres. The remaining Sr atoms are shown as large orange spheres.

3.3. FT–IR measurements

Fig. 4 illustrates the FT–IR spectra before and after thermal treatment. The most intense bands (615 and 390 cm^{-1}) were assigned to the antisymmetric stretching (ν_3) and antisymmetric bending (ν_4) modes, respectively, of the MoO_6 octahedron of the main phase $Sr_{11}Mo_4O_{23}$, according to previous reports of Mo-containing perovskites (Liegeois-Duyckaerts & Tarte, 1974). The band at 815 cm^{-1} is assigned to the ν_1 (symmetric stretching) mode of the MoO_4 tetrahedron of the $SrMoO_4$ impurity also detected by XRPD.

Additionally, as shown in Fig. 4, the characteristic bands of hydration water at 3430 and 1650 cm^{-1} can be identified before heating; the first one is assigned to the ν_1 (symmetric stretching) and ν_3 (antisymmetric stretching) modes, while the second band corresponds to ν_2 (bending mode). The characteristic symmetric stretching band of carbonate (ν_1) is

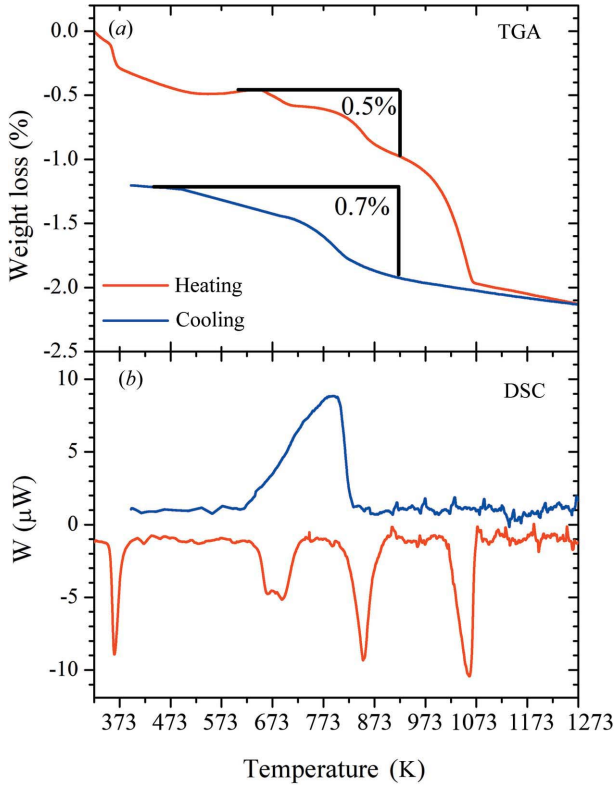

Figure 3
(*a*) Thermogravimetric analysis (TGA) and (*b*) differential scanning calorimetry (DSC) curves of $Sr_{11}Mo_4O_{23}$, measured in an air flow at a heating rate of 1 K min^{-1}.

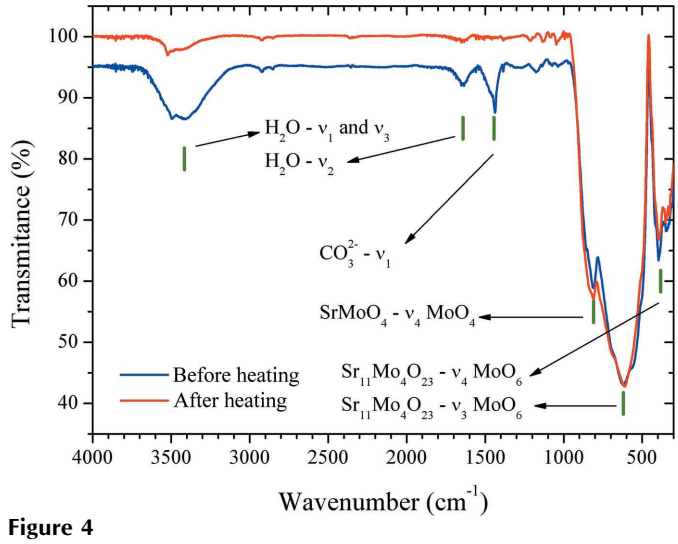

Figure 4
FT–IR spectra before and after thermal treatment. Green bars indicate the assigned normal vibrational modes.

observed at 1435 cm^{-1} (Nakamoto, 1997). However, in the FT–IR spectrum collected immediately after heating the sample, the carbonate band disappears and the water modes are strongly reduced.

3.4. Thermal expansion measurements

With the aim of determining the mechanical compatibility of our material with the other cell components, thermal expansion measurements were carried out in a dense ceramic. Fig. 5 shows a subtle change in the thermal expansion coefficient from 14.8 to 17.0 $\times 10^{-6}$ K^{-1} at low (423–673 K) and high (923–1223 K) temperatures, respectively. This change is coincident with the reversible mass-loss process between 673 and 848 K observed in TGA.

3.5. Conductivity measurements

Fig. 6(*a*) shows the conductivity measurements carried out in a dry air atmosphere. The observed conductivity can be interpreted as the mobility of oxide ions, since Mo is in its hexavalent oxidation state and there are no electronic charge carriers in this oxide. At the lowest measurement temperature, $T = 473$ K, the conductivity is $\sigma = 10^{-8}$ S cm^{-1}, but it increases with temperature and is particularly activated above 673 K, rising by several orders of magnitude. This is concomitant with the changes determined from the TGA and DSC measurements, involving an increment in the concentration of O vacancies. In the two extreme conduction regimes, below 523 K and above 773 K, the conductivity can be represented by $\sigma_T = \sigma_0 \exp(-Ea/kT)$, where Ea and k are the activation energy and the Boltzmann constant, respectively. From the plot of $\log(\sigma_T)$ *versus* T^{-1}, two activation energies are calculated: 0.47 and 0.63 eV in the low- and high-temperature regimes, respectively (Fig. 6*b*).

4. Discussion

As mentioned above, distorted double perovskites with a broken corner-sharing connectivity of the octahedral framework are mostly *A*-site deficient mixed oxides. The structures reported hitherto with *B* = Re or Os (Tomaszewska & Müller-Buschbaum, 1993; Jeitschko *et al.*, 1998; Bramnik *et al.*, 2000; Wakeshima & Hinatsu, 2005) present an $A_{11}B_4O_{24}$ formula, whereas for *B* = W (Hong, 2007) the formula is $A_{11}B_4O_{23}$. This difference in oxygen content is due to the valence of the *B* cations. The Re or Os compounds present a mixed-valence $B^{6+/7+}$ state, whereas for W the oxidation state is W^{6+}. For this reason the phase with Mo^{6+} studied here, similarly to W, also presents oxygen vacancies. Thus, the $Sr_{11}Mo_4O_{23}$ formula can be rewritten as $Sr_7\square(Sr_4Mo_4)O_{23}\square$, or as a double perovskite, $Sr_{1.75}\square_{0.25}(SrMo)O_{5.75}\square_{0.25}$. The oxygen content of 5.75 was computed from the charge balance of the compound, assuming that Mo is hexavalent. The structure may be regarded as a cation–vacancy ordered double perovskite structure, forming a novel superstructure.

This superstructure presents a tetragonal symmetry ($I4_1/a$) where the cell parameters are connected with the parameter of the simple cubic perovskite ABO_3 (a_0) as $a = b \simeq 2(2^{1/2})a_0$ and $c \simeq 4a_0$. For this crystallographic model, the Sr atoms are distributed over four different positions, Mo over two and O over six distinct sites. In Tables 1 and 2, Sr1, Sr2 and Sr3

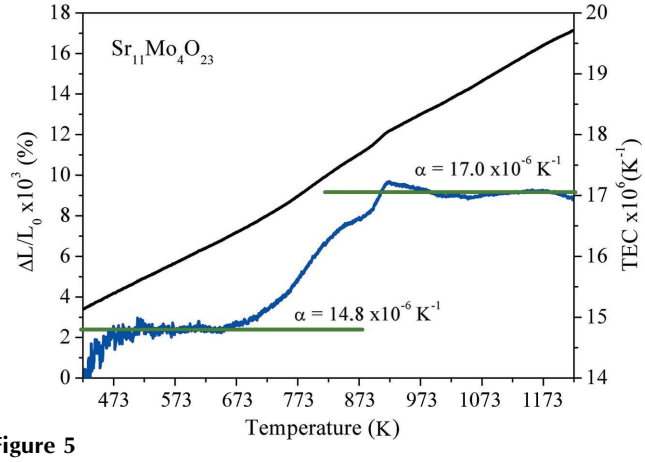

Figure 5
Thermal expansion measurements on $Sr_{11}Mo_4O_{23}$.

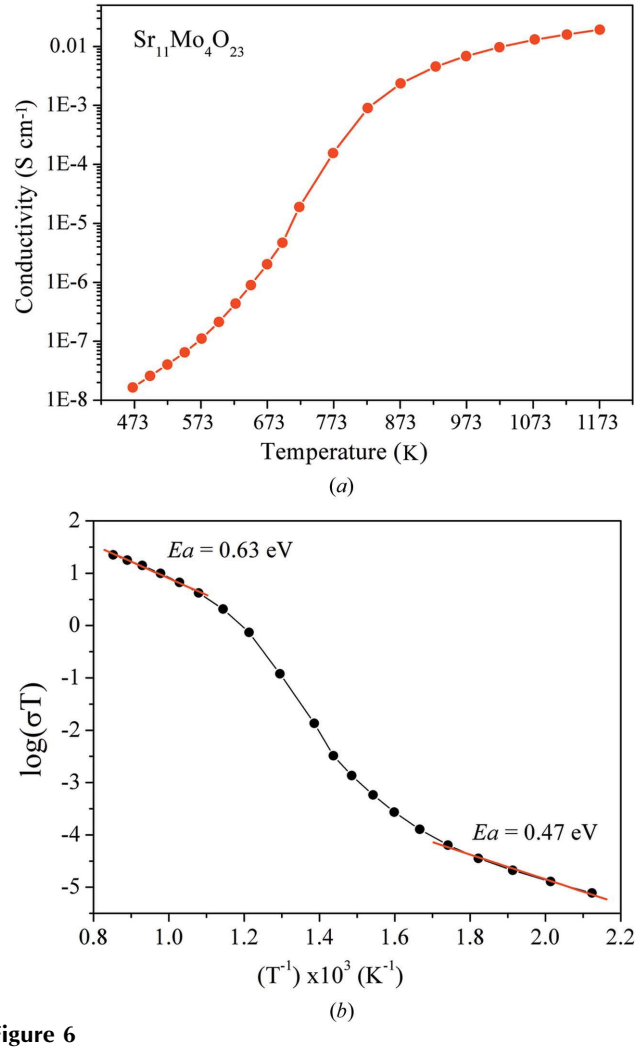

Figure 6
(*a*) Conductivity plotted as a function of temperature and (*b*) variation in $\log(\sigma_T)$ plotted *versus* the inverse of temperature (T^{-1}).

correspond to *A*-site cations exhibiting different coordinations ranging from 12 to 8, while Sr4, Mo1 and Mo2 correspond to *B*-site cations.

Fig. 2(*c*) shows that atoms Mo1, Mo2 and Sr4 occupy the *B* positions of the perovskite subcell in an ordered manner, forming a 'rock-salt' type cation sublattice. The Mo1 and Mo2 ions are coordinated by six oxide ions, forming MoO_6 octahedra, whereas the Sr4 ion is coordinated by eight O atoms, forming SrO_8 polyhedra. These polyhedra link the six neighbouring MoO_6 octahedra into a three-dimensional network by corner sharing and edge sharing, respectively (see Fig. 2*c*). In order to incorporate the SrO_8 polyhedra, the perovskite octahedral framework is significantly transformed. $Mo1O_6$ octahedra are only slightly tilted along [110], whereas $Mo2O_6$ octahedra are rotated along the same axis by ∼45°. As shown in Table 2, both $Mo1O_6$ and $Mo2O_6$ octahedra present the same average distances, 1.92 (1) Å, but the degree of distortion is completely different. It can be computed using the distortion index $\Delta(B-O)$ (Alonso *et al.*, 2000):

$$\Delta(B-\mathrm{O}) = \frac{1}{n}\sum_{n=1}^{n}\left[\frac{(B-\mathrm{O})_n}{\langle B-\mathrm{O}\rangle} - 1\right]^2, \qquad (1)$$

where $(B-\mathrm{O})_n$ and $\langle B-\mathrm{O}\rangle$ are the individual and average bond distances, respectively. The distortion index for $Mo1O_6$ is 0.47×10^{-4}, whereas for $Mo2O_6$ it is 21.35×10^{-4} (see Table 2). This increase in $Mo2O_6$ distortion happens because the Mo2—O4 distance (2.05 Å) is greater than Mo2—O5 (1.85 Å) and Mo2—O6 (1.87 Å). The Mo2 octahedra, indicated in green in Fig. 2, clearly show an axial distortion, where two of the O atoms (shown in yellow) are further apart from Mo than those of the equatorial plane. In assessing the O occupancies in the refinements, atom O4 shows a deficit of 22 (4)%. Furthermore, the O atoms of the equatorial plane exhibit very large displacement parameters, indicating a probable mobility within the structure. These vacancies and displacement parameters are directly related to the conductivity of the material. The stoichiometry found from the combined NPD and XRPD refinements is $Sr_{11}Mo_4O_{23.1\,(2)}$, in agreement with the expected formula $Sr_{11}Mo_4O_{23}$.

The thermal behaviour was investigated by TGA, DSC and FT–IR measurements, as described above. The irreversible changes are due to dehydration and decarbonation of the sample on the surface: this compound absorbs H_2O and CO_2 after a time, even when it is kept in a desiccator. As expected, both are endothermic processes. These changes are very subtle and correspond to 0.5 and 1% of the total weight of the sample. The hydration and carbonation were not detected by XRPD, but conspicuous bands were observed in FT–IR (3430 and 1435 cm^{-1}), assigned to water and carbonate vibrations, respectively (Fig. 4). As can be seen, the carbonate band disappears and the water vibration modes are strongly reduced after thermal treatment at 1273 K. For these reasons, we think that both the hydration and the carbonation are purely surface processes. It should be noted that, from consecutive TGA and FT–IR measurements, we found that the amount of water and carbonate remain constant one week after the synthesis. Reaction times of longer than one week did not produce changes in the samples, suggesting that the absorbed impurities reach an equilibrium with the atmosphere after this time.

A more interesting reversible process is observed between 673 and 873 K. Upon heating, it consists of two well defined endothermic weight losses (at 673 and 853 K), while on cooling two exothermic processes of mass gain are observed, although these are broader than in the heating run. This complex reversible process is attributed to a change in the oxygen content of the sample. This change is abrupt during heating but smoother on cooling. This suggests that the loss of oxygen is rapid but the reoxidation process is slow. The loss of oxygen corresponds to 0.5%, which represents 0.54 atoms per formula unit. We can propose the following equilibrium equation:

$$Sr_{11}Mo_4O_{23.1\,(2)} \leftrightarrow Sr_{11}Mo_4O_{22.5}, \qquad (2)$$

which implies the partial reduction of Mo^{6+} to Mo^{5+}.

This change in the oxygen content is also observed in the thermal expansion measurements, where the TEC increases from 14.8 to 17.0 $\times 10^{-6}$ K^{-1} in the temperature range 673–873 K as the oxygen content changes. The calculated values of the TEC are within the range of those usually displayed by SOFC electrolytes.

The conductivity is also influenced by the change in oxygen content. As can be seen in Fig. 6(*a*), the conductivity is moderate, but with the loss of oxygen it increases by approximately three orders of magnitude. It is remarkable that such a subtle change in oxygen content affects the overall ionic mobility so strongly. The partial reduction of Mo^{6+} to Mo^{5+}

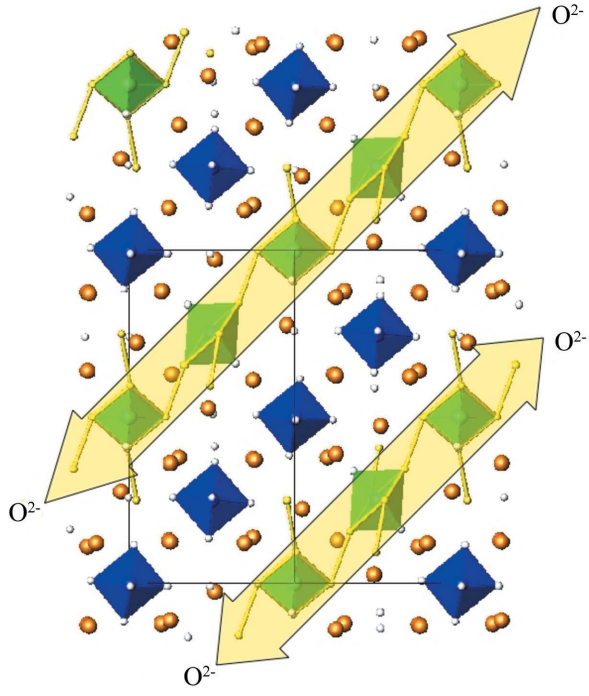

Figure 7
Scheme of the probable O^{2-} ion mobility pathways in the structure, indicated by yellow shading.

probably leads to localized Mo^{5+} ions, and therefore it is implausible that this contributes to the electronic conductivity. Crystallographically, the more labile O atoms are those constituting the $Mo2O_6$ octahedron, *i.e.* O4, O5 and O6. Table 1 shows that atom O4 presents a deficiency of 22% and atoms O5 and O6 display large displacement parameters, which are unrealistic. This suggests that the mobility of oxygen is based upon these three atoms. Fig. 7 shows a scheme of the probable O^{2-} ion mobility in the structure.

The plot of $\log(\sigma_T)$ *versus* T^{-1} shows linear behaviour below 523 and above 773 K, with activation energies of 0.47 and 0.63 eV, respectively (see Fig. 6*b*). These values are slightly lower than those found in phases with similar stoichiometry (Ha *et al.*, 2008) and in conventional electrolytes such as $Gd_2Ti_2O_7$, YSZ and lanthanum strontium gallate magnesite (LSGM) (Kramer & Tuller, 1995; Yoo & Hwang, 1992; Kim & Yoo, 2001). Regarding the conductivity, the $Sr_{11}Mo_4O_{23}$ electrolyte presents a moderate ionic conductivity. These values are lower than for YSZ at 1273 K and LSGM at 1073 K (Yoo & Hwang, 1992; Kim & Yoo, 2001), but are close to that of gadolinium-doped ceria above 873 K, which is itself a promising material for IT-SOFC applications (Steele, 2000; Sikalidis, 2011).

5. Conclusions

The novel $Sr_{11}Mo_4O_{23}$ oxide, a derivative of double perovskites with a broken corner-sharing connectivity of the octahedral framework, is found to present *A*-site and O vacancies, as shown from a neutron diffraction study. It presents a reversible process of removal/uptake of O-atom content in the 673–873 K temperature range. This change was observed by TGA and DSC techniques and in the thermal expansion. The conductivity is strongly activated after the topotactic removal of 0.54 O atoms per formula unit. This material performs as an oxide ion conductor, with a moderate ionic conductivity compared with conventional electrolyte oxides. This phase constitutes an interesting starting point for designing structurally related derivative materials, with suitable chemical doping designed to promote an enhanced ionic conductivity.

JCP thanks CONICET (project Nos. PIP01360/08 and PIP00912/12) and SECyT-UNSL (project Nos. PROICO7707 and PROICO2-1612). DGL acknowledges ANPCyT for financial support (projects PICT2011 Nos. 1948 and 2689). CAL, JCP and DGL are members of CONICET. JAA thanks the Spanish MICINN for funding *via* project No. MAT2013-41099-R. We are grateful to PSI for making the neutron beamtime available.

References

Abakumov, A. M., King, G., Laurinavichute, V. K., Rozova, M. G., Woodward, P. M. & Antipov, E. V. (2009). *Inorg. Chem.* **48**, 9336–9344.
Alonso, J. A., Martínez-Lopez, M. J., Casais, M. T. & Fernández-Díaz, M. T. (2000). *Inorg. Chem.* **39**, 917–923.
Bramnik, K., Miehe, G., Ehrenberg, H., Fuess, H., Abakumov, A., Shpanchenko, R., Pomjakushin, V. & Balagurov, A. (2000). *J. Solid State Chem.* **149**, 49–55.
Graves, C., Sudireddy, B. R. & Mogensen, M. (2010). *ECS Trans.* **28**, 173–192.
Ha, J., Lee, E., Hong, S. & Yoo, H. (2008). *Solid State Ionics*, **179**, 1066–1070.
Hong, S. (2007). *J. Solid State Chem.* **180**, 3039–3048.
Jeitschko, W., Moens, H. A., Rodewald, U. C. & Möller, M. H. (1998). *Z. Naturforsch. Teil B*, **53**, 31–36.
Kartha, S. & Grimes, P. (1994). *Phys. Today*, **47**, 54–61.
Kim, J.-H. & Yoo, H.-I. (2001). *Solid State Ionics*, **140**, 105–113.
King, G., Abakumov, A. M., Hadermann, J., Alekseeva, A. M., Rozova, M. G., Perkisas, T., Woodward, P. M., Van Tendeloo, G. & Antipov, E. V. (2010). *Inorg. Chem.* **49**, 6058–6065.
Kramer, S. A. & Tuller, H. L. (1995). *Solid State Ionics*, **82**, 15–23.
Lacorre, P., Goutenoire, F., Bohnke, O., Retoux, R. & Laligant, Y. (2000). *Nature*, **404**, 856–858.
Liegeois-Duyckaerts, M. & Tarte, P. (1974). *Spectrochim. Acta Part A*, **30**, 1771–1786.
Nakamoto, K. (1997). *Infrared and Raman Spectra of Inorganic and Coordination Compounds*, 5th ed. New York: John Wiley and Sons.
Rao, C. N. R. & Raveau, B. (1998). *Transition Metal Oxides: Structure, Properties, and Synthesis of Ceramic Oxides.* New York: John Wiley and Sons.
Raveau, B. (2007). *Prog. Solid State Chem.* **35**, 171–173.
Rietveld, H. M. (1969). *J. Appl. Cryst.* **2**, 65–71.
Rodríguez Carvajal, J. (1993). *Physica B*, **192**, 55–69.
Sikalidis, C. (2011). Editor. *Advances in Ceramics – Synthesis and Characterization, Processing and Specific Applications*, ch. 19. Rijeka: InTech.
Singhal, S. C. & Kendal, K. (2003). *High-Temperature Solid Oxide Fuel Cells: Fundamentals, Design and Applications*. Amsterdam: Elsevier.
Steele, B. (2000). *Solid State Ionics*, **129**, 95–110.
Steele, B. C. & Heinzel, A. (2001). *Nature*, **414**, 345–352.
Tomaszewska, A. & Müller-Buschbaum, H. (1993). *Anorg. Allg. Chem.* **619**, 1738–1742.
Wakeshima, M. & Hinatsu, Y. (2005). *Solid State Commun.* **136**, 499–503.
Yoo, H. & Hwang, J. (1992). *J. Phys. Chem. Solids*, **53**, 973–981.